Fuel 275 (2020) 117879

Contents lists available at ScienceDirect

Fuel

journal homepage: www.elsevier.com/locate/fuel

Full Length Article

Derivation of oxygen-containing functional groups on biochar under non-oxygen plasma for mercury removal

Huicong Zhang[a], Tao Wang[a,*], Wei-Yin Chen[b], Yongsheng Zhang[a,*], Baomin Sun[a], Wei-Ping Pan[a]

[a] Key Laboratory of Power Station Energy Transfer Conversion and System, Ministry of Education, North China Electric Power University, Beijing 102206, PR China
[b] Department of Chemical Engineering, University of Mississippi, 134 Anderson Hall, University, MS 38677, USA

GRAPHICAL ABSTRACT

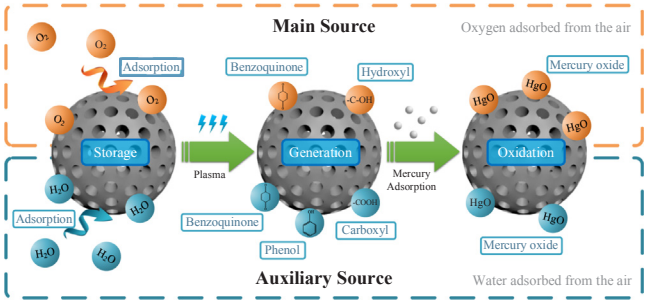

ARTICLE INFO

Keywords:
Plasma
Biochar
Water
Oxygen
Functional group
Mercury removal

ABSTRACT

Biochar was subjected to N_2-plasma treatment after adsorbing water or oxygen. The mercury removal efficiency of the obtained samples was tested. The results of H_2O-thermogravimetric and O_2-temperature programmed desorption show that biochar had adsorption capacity for both water and oxygen during storage. The adsorbed water exhibited an inhibitory effect on mercury removal. However, after plasma treatment, water decomposed into oxygen-containing active radicals and combined with biochar to form oxygen-containing functional groups. The generated functional groups compensated for the inhibition of mercury capture. After the biochar adsorbed oxygen, the biochar was easily sintered under plasma, thereby reducing the mercury removal performance. The oxygen-containing functional groups formed by plasma treatment of oxygen adsorbed biochar also improved the mercury removal efficiency. Hg-temperature programmed desorption revealed that Hg^0 could be oxidised by the generated oxygen-containing functional group to form HgO. Correlation analysis showed that the oxygen adsorbed by the biochar from air during storage was the main source of oxygen-containing functional groups generated under a non-oxygen plasma environment. The correlation coefficient was up to 0.999. During normal storage, the oxygen adsorbed by the adsorbent from the air can be converted into oxygen-containing functional groups during the plasma modification process, thereby oxidising Hg^0.

1. Introduction

At present, plasmas are used in many applications or tools, such as inductively coupled plasma mass spectrometry, coating, etching, and modification [1–4]. In plasma, gas molecules are in an ionised state, making it easier to obtain the desired molecular fragments [5]. Biochar is a cheap and easily available adsorbent [6,7]. In our previous studies, chlorine and hydrogen sulphide were used as plasma-modified gases to

* Corresponding authors.
E-mail addresses: wtao@ncepu.edu.cn (T. Wang), yszhang@ncepu.edu.cn (Y. Zhang).

https://doi.org/10.1016/j.fuel.2020.117879
Received 18 September 2019; Received in revised form 14 March 2020; Accepted 15 April 2020
Available online 23 April 2020

activate biochar [8–10]. The obtained biochar was used for mercury removal. During the process of plasma modification, it was considered that the formed C-Cl or C-S was the main functional group for mercury removal. The form of mercury produced was mainly $HgCl_2$ or HgS. However, an analysis of the mercury species revealed that a small amount of HgO was also present in the modified sample after adsorption. Moreover, it was found by X-ray photoelectron spectroscopy (XPS) that the proportion of oxygen-containing functional groups on the surface of the biochar was increased after plasma modification.

Oxygen-containing functional groups can promote mercury removal [11]. Zhang and Bohli [12,13] pointed out that oxygen-containing functional groups can oxidise Hg^0 to form HgO. The increased amount of oxygen-containing functional groups should be a combination of active free radicals formed from oxygen-containing molecules in the plasma environment and biochar, but the modified gas is Cl_2 or H_2S and the carrier gas is N_2. Thus, there is no source of oxygen in the modified gas. Similar situations have occurred in other plasma applications. Yang et al. [14] found that oxygen-containing functional groups were increased after N_2 plasma treatment. Majumdar et al. [15] also indicated that oxygen-containing functional groups were enhanced after CH_4/N_2 dielectric barrier discharge (DBD) plasma. Nevertheless, the study did not indicate the source of these oxygen functional groups, and the modified gas did not contain oxygen. Thus, oxygen is likely to come from oxygen or water physically adsorbed by the biochar itself. Since oxygen-containing functional groups promote the removal of mercury, oxygen-containing functional groups generated in a non-oxygen plasma environment cannot be ignored. Therefore, exploring the source of oxygen-containing functional groups on biochar after non-oxygen plasma treatment is very important for plasma modification methods and mercury removal. The main source of oxygen-containing functional groups generated in non-oxygen plasma, i.e. physically adsorbed oxygen or water, needs to be clarified. The effect of physically adsorbed water or oxygen on mercury removal after plasma modification also needs to be studied. This study could also improve the mechanism of mercury capture by modified biochar using plasma.

In this study, biochar was subjected to plasma modification after adsorbing oxygen and water. The mercury removal performance of the sample was also tested. The adsorption capacity of biochar for water and oxygen was explored by H_2O-thermogravimetric (H_2O-TG) and O_2-temperature programmed desorption (O_2-TPD). The functional groups were identified using Fourier transform infrared spectroscopy (FTIR). The variation in the binding energy of carbon and oxygen was measured using X-ray photoelectron spectroscopy (XPS). The speciation of captured mercury was specified using Hg-temperature programmed desorption (Hg-TPD).

2. Materials and methods

2.1. Biochar preparation

The biochar was derived from rice straw. The rice straw was collected from Huainan, Anhui Province, China. After the straw was pulverised, it was washed three times with deionised water and dried in a drying oven (80 °C) for 48 h. About 20 g of biomass powder was placed in a 30 cm corundum boat, then the boat was placed in a 50 mm tube furnace and pure nitrogen was introduced at a flow rate of 500 mL/min. After the pure nitrogen gas had been introduced for 10 min, the furnace began to heat up. The temperature was raised from room temperature to 900 °C at 10 °C/min and held at 900 °C for 1 h. Subsequently, the furnace stopped heating and was cooled to room temperature. Biochar prepared at 900 °C minimises the physical adsorption of water and oxygen. After pyrolysis, the biochar sample was sieved through 200–350 mesh before the experiment. The obtained biochar was designated as RB.

2.2. Modification of biochar

In order to explore the effects of physically adsorbed water and oxygen on plasma modification, the biochar was artificially adsorbed with varying amounts of water and oxygen. Dissolved oxygen in ionic water was removed by a N_2 purge before modification. The purity of nitrogen used in the experiment was 99.999%, and an adsorbent was installed at the outlet of the nitrogen bottle to remove traces of oxygen and water from the gas. First, water adsorption was carried out using 500 mL/min pure nitrogen into a gas cylinder filled with deionised water. The gas cylinder was placed in a water bath at 50 °C to heat. The water vapour (7%) carried by pure nitrogen was passed through a heating trace pipe (100 °C) to a plasma reactor (DBD-100A, Nanjing Suman Plasma Technology Co., Ltd.) containing 0.3 g of biochar. After the biochar had adsorbed the water vapour for 10–180 min, the gas path was switched to pure nitrogen. Then, the sample was modified in a plasma environment. The discharge voltage was 8 kV, the flow rate of N_2 was 500 mL/min and the plasma treatment time was 5 min. The model of the plasma generator was ATP 2000 K (Nanjing Suman Plasma Technology Co., Ltd.). The water-adsorbed plasma-modified sample was designated RB-H-X (X is the adsorption time).

For oxygen-adsorbed plasma modification, the oxygen concentration was set to 7% by adjusting the ratio of pure nitrogen to oxygen. The total gas flow rate was maintained at 500 mL/min. The adsorption of oxygen onto biochar was followed the same step as that of water absorption process. The biochar adsorbed oxygen for different periods of time and was then treated by plasma at 500 mL/min of pure nitrogen. The plasma modification parameters were the same as above. The oxygen-adsorbed plasma-modified sample was designated RB-O-X (X is the adsorption time). The samples that only adsorbed water or oxygen without plasma treatment were designated as RB-H/O-X-NP. The schematic of the modification device is shown in Fig. 1. Details of the modified samples are shown in Table 1.

2.3. Biochar characterisation

The functional groups of biochar before and after modification were characterised by FTIR (Frontier, PerkinElmer, America). The functional groups on the surface of the sample appear on the spectrum as peaks after FTIR testing. The peaks of different functional groups appear in different wavenumber ranges, so that the types of functional groups can be identified. The infrared spectrum scanning range was from 450 to 4000 cm^{-1}. The changes in the elemental state of biochar were revealed by XPS (ESCALAB 250Xi, Thermo Fisher Scientific, America). The valence transition of C, O and N was reflected by the change in binding energy. By comparing the changes of the element states before and after the reaction, the mechanism of the reaction process can be inferred. Hg-TPD was used to distinguish the species of mercury adsorbed onto the biochar. By heating the adsorbed sample in a N_2 environment, different forms of Hg were released at different temperatures. The Hg-TPD experiment was increased from 30 to 600 °C, the amount of sample after Hg^0 adsorption was 0.1 g and the N_2 flow rate was 500 mL/min. The release signal value of mercury was detected by Lumex RA915 apparatus (Lumex Inc. Canada). The adsorption capacity of biochar for water (H_2O-TG) was detected by PSA Q5000 SA (P S Analytical, United Kingdom). This instrument can record the weight of biochar as it changes with the time of H_2O adsorption. For this, 5 mg of biochar was placed on the balance of the instrument and then heated to a constant weight at 60 °C in N_2. After that, pure nitrogen containing 7% water was introduced to the balance at 30 °C and the weight change of the balance was recorded. The adsorption capacity of biochar for oxygen (O_2-TPD) is carried out on a TPD/TPR dynamic adsorption instrument (TP-5076, Xianquan Industrial and Trading Co., Ltd.) [16]. For this, 50 mg of biochar was first pretreated in helium atmosphere at 150 °C for 2 h. Oxygen was then introduced and the biochar was adsorbed in an oxygen environment for different periods of time at 30 °C.

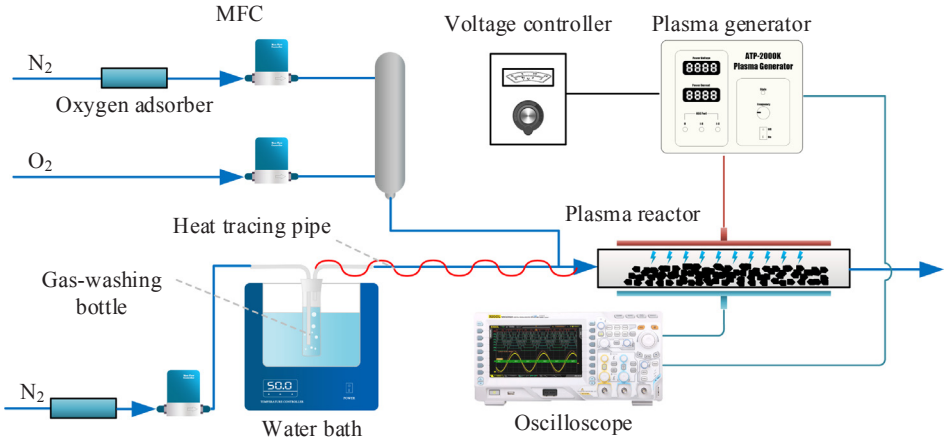

Fig. 1. The schematic of modification device.

Table 1
Details of the modified sample.

Name	H_2O	O_2	Adsorption Time (min)				Plasma treatment
			10	30	60	180	
RB	–	–	–	–	–	–	–
RB-H-10	√	–	√	–	–	–	√
RB-H-30	√	–	–	√	–	–	√
RB-H-60	√	–	–	–	√	–	√
RB-H-180	√	–	–	–	–	√	√
RB-H-180-NP	√	–	–	–	–	√	–
RB-O-10	–	√	√	–	–	–	√
RB-O-30	–	√	–	√	–	–	√
RB-O-60	–	√	–	–	√	–	√
RB-O-180	–	√	–	–	–	√	√
RB-O-180-NP	–	√	–	–	–	√	–

After the adsorption of oxygen, helium was used to purge 5 min. Then, the biochar was heated from 30 °C to 850 °C at a heating rate of 10 °C/min in a helium atmosphere. The gas desorbed during the temperature rise was detected by the instrument.

2.4. Mercury adsorption

The mercury adsorption experiment was carried out on a fixed bed. The fixed bed was a 250 mm long quartz tube with an inner diameter of 6 mm. The elemental mercury source was supplied by CAVKIT Hg Calibration (PSA 10.536). The elemental mercury concentration could be adjusted by the computer directly, and the mercury concentration in the experiment is set to 20 μg/m^3. After adsorption, the concentration of mercury in the gas was detected by a SIR GALAHAD II instrument (PSA 10.525). In this experiment, 50 mg of the sample was placed in a fixed bed, and both sides were fixed by quartz wool. The temperature of the fixed bed was controlled by the oven box and maintained at 150 °C. The total experimental gas flow rate was 1 L/min. The Hg^0 concentration was tested every 5 min. The experimental diagram of the fixed bed can be seen in our previous study [8]. Each experiment was repeated three times and the results were averaged.

The Hg^0 adsorption efficiency was calculated by the following equation [17–21].

$$\eta = \frac{C_{in} - C_{out}}{C_{in}} \times 100\% \quad (1)$$

where η is the removal efficiency of Hg^0 removal (%), C_{in} is the inlet concentration of mercury in the fixed bed (μg/m^3) and C_{out} is the outlet concentration of mercury in the fixed bed (μg/m^3).

3. Results and discussion

3.1. H_2O-TG and O_2-TPD analysis

When a material is not in a vacuum environment, the material will absorb some of the gas in the surrounding environment. Most materials are exposed to the air when they are stored. Therefore, moisture and oxygen in the air are often absorbed into the material. Therefore, before the biochar is subjected to mercury removal experiments and characterisation, the adsorption capacity of water and oxygen needs to be determined.

As shown in Fig. 2, the ability of biochar to adsorb water is obvious. In the first 30 min of adsorbing water, the weight of biochar increased by 8.27%. In the next 150 min, the weight was still increasing, but the growth rate was slower. For samples adsorbed at different times, the weight of RB-H-10, RB-H-30, RB-H-60 and RB-H-180 increased by 7.35%, 8.27%, 8.75% and 9.19%, respectively. As the adsorption time increased, the weight increase rate slowed down. This indicates that biochar has a good adsorption capacity for water and can be saturated under long-term adsorption. Fig. 3(a) shows the O_2-TPD curves under different O_2 adsorption time. There was a desorption peak in the biochar after oxygen adsorption at 30 °C to 130 °C. This peak was attributed to the release of oxygen adsorbed on the surface of the biochar [22–25]. Moreover, as the time for oxygen adsorption increased from 10 min to 180 min, the area of the desorption peak increased from 76.9 to 140.4. According to Fig. 3(b), the weight of the biochar increased by 0.34% after 10 min of oxygen adsorption. The weight of biochar increased from 0.34% to 0.54% when the adsorption time was increased from 10 min to 180 min. This shows that biochar has oxygen adsorption capacity at room temperature, and it has a significant release peak at

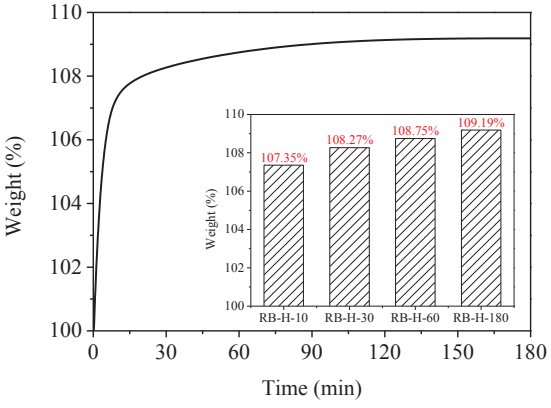

Fig. 2. H_2O-TG curves under different H_2O adsorption time.

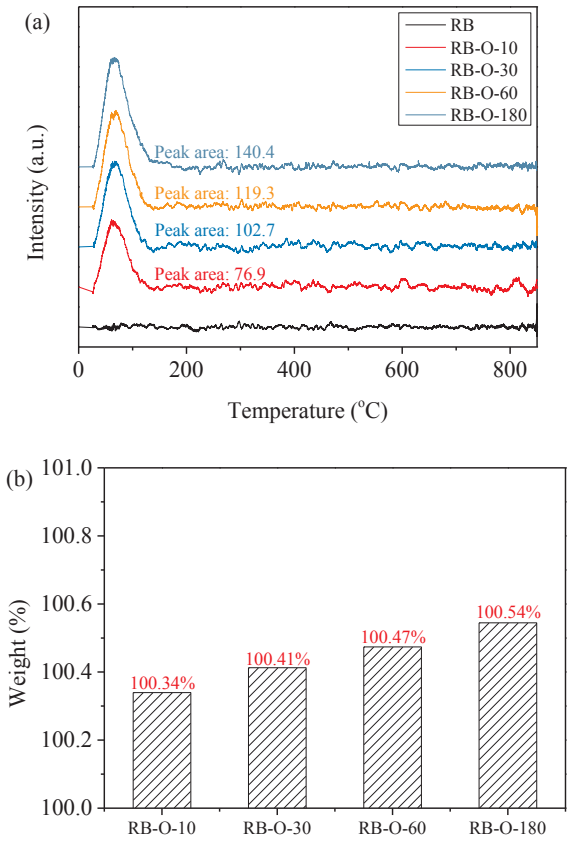

Fig. 3. (a) O_2-TPD curves under different O_2 adsorption time and (b) weight gain ratio at different times of adsorbed O_2.

around 100 °C. This provides a good basis for the storage of oxygen in biochar.

In summary, biochar has an adsorption capacity for both water and oxygen. Under normal storage, biochar easily absorbs 21% of the oxygen in the air or the water with varying concentrations. The presence of water and oxygen in the biochar can provide a source of oxygen for plasma modification to form oxygen-containing functional groups.

3.2. Adsorption performance

The mercury removal effect is shown in Fig. 4. The initial efficiency of mercury removal from RB was about 5.7%. The H_2O-adsorbed biochar after plasma modification exhibited inhibited mercury removal. The initial efficiency of the modified sample adsorbed for 10 min of water decreased slightly from 5.6% to 5.3%. As the time to adsorb water increased from 10 min to 180 min, the initial efficiency decreased from 5.3% to 2.6%. All samples modified with adsorbed water showed the inhibition of mercury removal. This inhibition may come from two sources. One is due to the etching effect of the plasma on the biochar, which leads to a decrease in the adsorption performance of the biochar [9,26]. The plasma has high energy that bombards the surface of the material. This causes an etching phenomenon. The other is that a high water concentration will occupy the adsorption sites of the biochar surface and reduce the amount of mercury adsorbed. The mercury removal efficiency of RB-H-180-NP was 1.5% lower than that of RB-H-180. This indicates that plasma modification is promoted for the mercury removal performance of the sample. The oxygen-containing functional groups generated by the H_2O plasma may compensate for the inhibition of mercury removal.

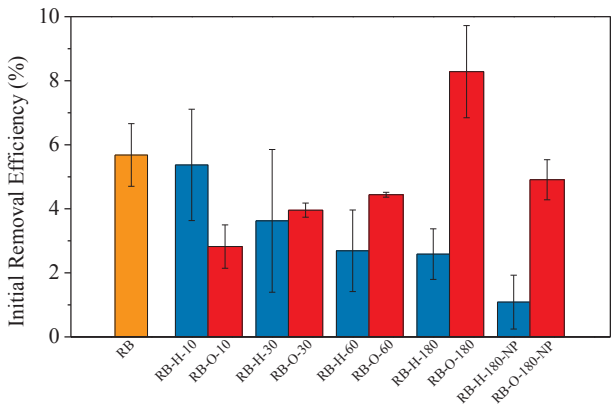

Fig. 4. The mercury removal efficiency of samples.

For O_2-adsorbed biochar, initial efficiency decreased from 5.6% to 2.8% after 10 min of oxygen adsorption. However, as the oxygen adsorption time increased, its efficiency was gradually enhanced. When the oxygen adsorption time was increased from 10 min to 180 min, the efficiency increased from 2.8% to 8.3%. The decrease in efficiency of oxygen adsorption for 10 min could be due to structural etching of the biochar by the plasma. Moreover, the adsorption of oxygen promoted the sintering of the biochar surface in the plasma environment. Therefore, changes in the biochar structure resulted in a decrease in the active sites for mercury removal. When the oxygen adsorption time was prolonged, the amount of oxygen adsorbed on the biochar also increased, and more functional groups were formed under the plasma environment. The structural change caused by the plasma was compensated for as the number of oxygen-containing functional groups increased. Compared to RB-O-10, the efficiency reduction of RB-H-10 was not obvious. This may be due to the fact that the surface after adsorption of oxygen promoted sintering under plasma. Water may have a certain cooling effect. Similar to the sample adsorbed by water, the mercury removal efficiency of RB-O-180-NP was 3.4% lower than that of RB-O-180. This also suggests that plasma is a factor in improving the performance of mercury removal.

3.3. Hg-TPD analysis

Five samples, i.e. RB, RB-O-180-NP, RB-O-180, RB-H-180-NP and RB-H-180, were selected for Hg-TPD. This was to investigate the morphological changes of adsorbed Hg in biochar before and after modification. The TPD results are shown in Fig. 5. For RB, the TPD curve only showed a peak around 210 °C. This was attributed to the physical adsorption of Hg^0 [27,28]. This indicates that the adsorption of mercury by unmodified biochar (RB) was mainly via physical adsorption. For RB-H-180-NP, the desorption peak of TPD was also only the physically adsorbed Hg^0. However, the peak intensity was lower than RB, which indicated that water treated biochar decreased the mercury capture efficiency. This may have been because the water molecules occupied mercury adsorption active sites on the surface of the biochar and caused the reduction in efficiency without plasma treatment. The mercury desorption peak (RB-H-180) had a shoulder around 300 °C in the case of water and plasma treatment. Thus, the mercury desorption peak contained two subgroup peaks. The blue curve represents elemental mercury and the orange curve represents oxidised mercury at a higher temperature. The peak at 300 °C represents HgO formed by the combination of oxygen-containing functional groups and Hg^0 [29,30]. Therefore, after the water on the biochar was subjected to plasma treatment, oxygen-containing functional groups were formed on the surface of the biochar, such that Hg^0 could be oxidised.

For RB-O-180-NP, two mercury species appeared on the TPD curve. The blue curve at the lower temperature is Hg^0. The orange and green curves are HgO. Interestingly, the peak of HgO appeared in the temperature range of 400–550 °C [27,31]. Moreover, the peak of HgO was present in two adjacent peaks. The HgO peak in this temperature range

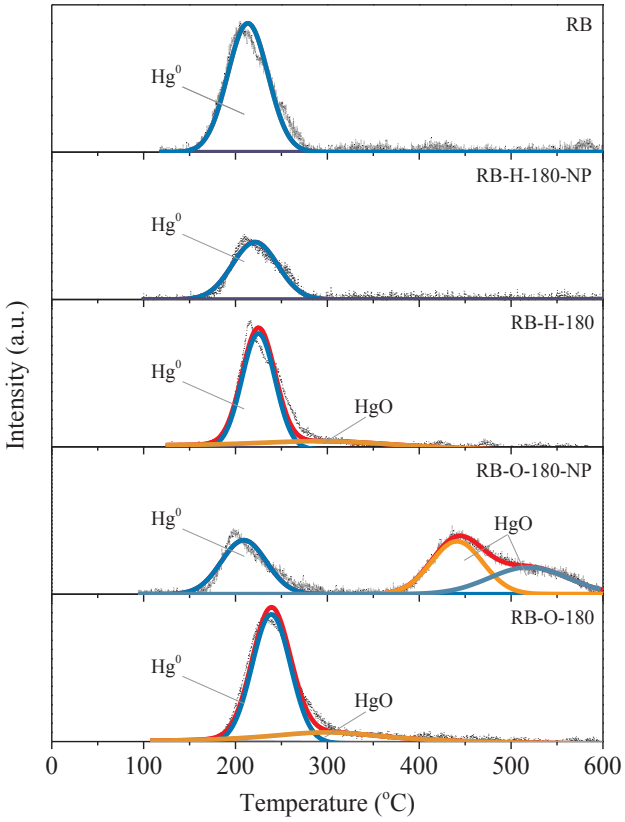

Fig. 5. TPD curves of samples after Hg^0-adsorption.

was formed by the oxidation of Hg^0 by oxygen adsorbed on the surface of the biochar [32]. Since HgO has two different lattice forms, there were two adjacent release peaks. For RB-O-180, the HgO peak in the high temperature range did not appear. Instead, a HgO peak at 300 °C appeared. This indicates that oxygen-containing functional groups were formed on the oxygen adsorbed biochar after plasma treatment, thereby oxidising Hg^0. The adsorbed oxygen was decomposed into oxygen-containing radicals after plasma treatment, and combined with biochar to form oxygen-containing functional groups. The HgO release peaks at two different temperatures also indicate the difficulty of mercury oxidation. The two different peak curves may be due to the different binding energies of elemental mercury with biochar to cause the differential formation of oxidised mercury. A low temperature release peak means less binding energy. This indicates that the oxygen-containing functional groups preferentially oxidised mercury, not the physically adsorbed oxygen. Therefore, the oxygen-containing functional groups that formed after plasma treatment improved the mercury removal efficiency of the biochar.

In general, for samples that were treated with plasma after H_2O and O_2 adsorption (RB-H-180 and RB-O-180), the peak of oxidation of Hg^0 by the oxygen-containing functional group appeared at 300 °C. At the same time, the desorption peak of Hg^0 slightly shifted to a high temperature range. This was due to the fact that the coexistence of two forms of mercury caused the desorption temperature to shift [29]. It suggests that, after the modification, oxygen-containing functional groups were generated on the biochar, thereby oxidising Hg^0 to HgO. This phenomenon is the same as that found in the Cl_2 and H_2S plasmas. In our previous studies, Hg-TPD of H_2S and Cl_2 plasma (non-oxygen atmosphere) modified samples also showed peaks of HgO at 300 °C [8]. Therefore, the physical adsorption of water and oxygen in biochar can increase the ability to oxidise mercury after plasma modification.

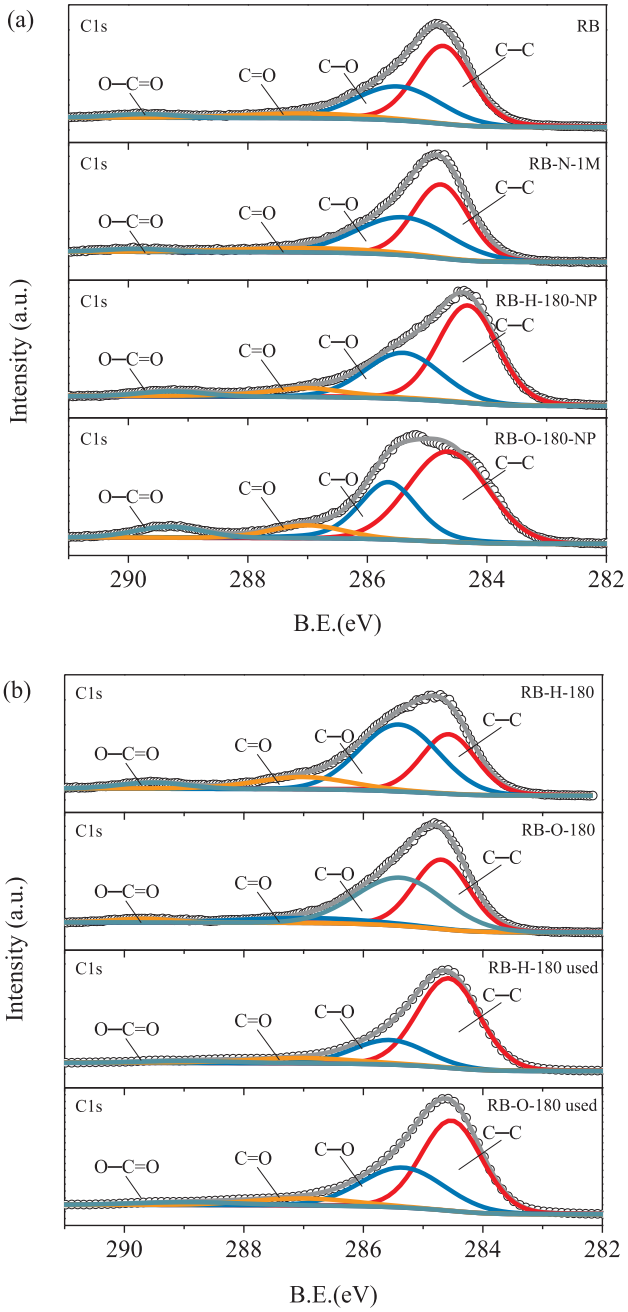

Fig. 6. C1s of XPS curves for different samples. (a) the fresh samples; (b) the samples after Hg^0 adsorption.

3.4. XPS analysis

For XPS, the area of binding energy between 282 and 291 eV is attributed to C1s. As shown in Fig. 6, four different peaks appear on the XPS results. The four peaks are located at 284.7, 285.4, 287.0 and 288.8 eV, which correspond to C–C, C–O, C═O and O–C═O, respectively [12,33–37]. The proportion of each peak area is shown in Table 2. For RB, the area of the C–C peak was the largest, accounting for 56.9% of the total area, and the proportion of all oxygen-containing functional groups was 43.1%. For RB after water or oxygen absorption, the ratio of C–C to oxygen-containing functional groups hardly changed. The proportion of the C–C peaks of RB-H-180-NP and RB-O-180-NP was maintained at 55.6% and 56.7%, respectively. This indicates that the amount of oxygen-containing functional groups on the surface of biochar did not increase after simply adsorbing water and

Table 2
The data of XPS analysis of C1s for samples.

Position (eV)	Area of samples (%)							
	RB	RB-N-1M	RB-H-180	RB-O-180	RB-H-180 used	RB-O-180 used	RB-H-180-NP	RB-O-180-NP
284.7(C–C)	56.9	49.6	33.3	43.9	67.8	56.3	55.6	56.7
285.4 (C–O)	33.7	40.9	50.7	46.5	21.7	33.5	32.7	29.8
287.0 (C═O)	6.8	7.4	12.1	7.2	8.3	7.3	8.8	7.6
288.8(O–C═O)	2.6	2.1	3.9	2.3	2.1	2.9	2.9	5.9

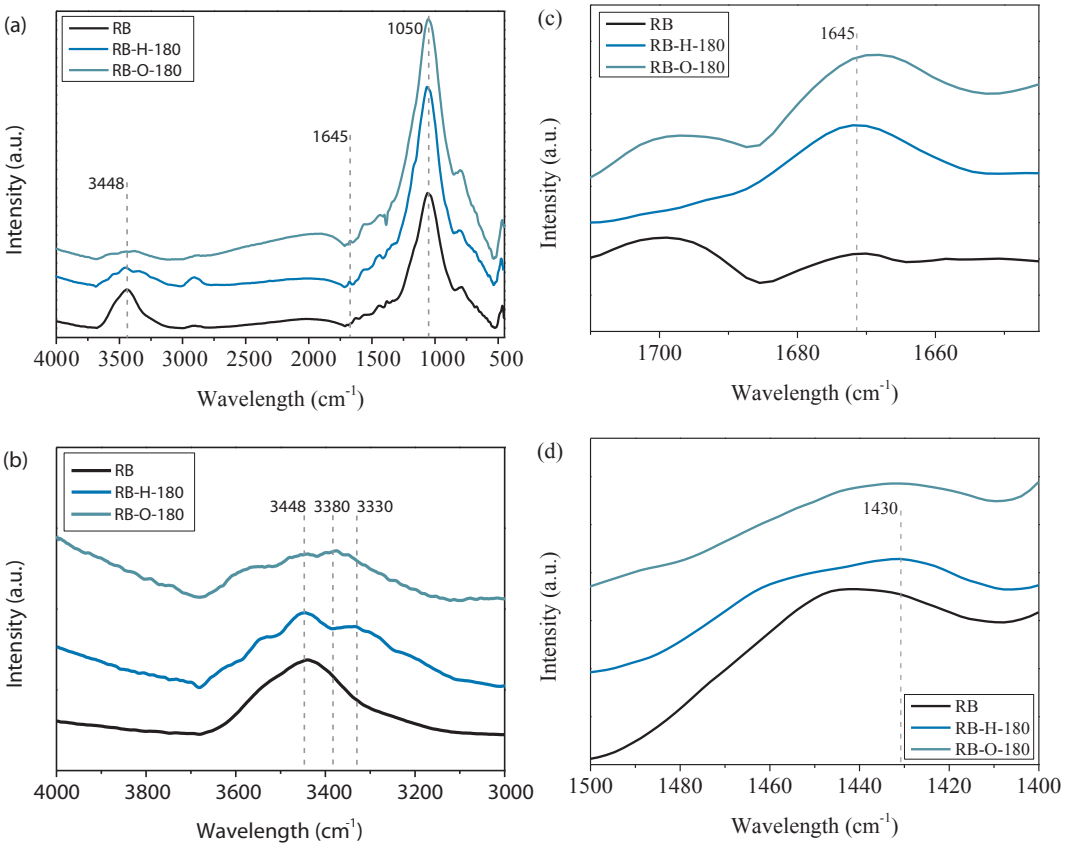

Fig. 7. FTIR spectra of samples, (a) the full spectrum, (b) zoom in at 4000–3000 cm^{-1}, (c) zoom in at 1710–1645 cm^{-1}, (d) zoom in at 1495–1400 cm^{-1}.

oxygen. Water and oxygen are only physically adsorbed on the surface of the biochar. The absence of an increase in oxygen-containing functional groups resulted in the inability to oxidise Hg, which is consistent with the TPD results.

However, for the plasma-modified samples (RB-H-180 and RB-O-180), the oxygen-containing functional groups varied greatly. The peak proportions of C–C of RB-H-180 and RB-O-180 were 33.3% and 43.9%, respectively. Compared with RB, the proportion of C–C decreased by 23.6% and 13.0%, separately. A decrease in the proportion of C–C indicates an increase in oxygen-containing functional groups. This means that after plasma treatment, water and oxygen can combine with biochar to form oxygen-containing functional groups. For RB-H-180, the proportion of the three oxygen-containing functional groups all increased. The ratios of C–O, C═O and O–C═O increased by 17.0%, 5.3% and 1.3%, respectively. For RB-O-180, only the proportion of C–O and C═O increased by 12.8% and 0.4%. The proportion of O–C═O hardly changed. Therefore, water and oxygen are different in the plasma environment for the formation of oxygen-containing functional groups on biochar. In a plasma environment, water forms three functional groups, i.e. C–O, C═O and O–C═O, on the surface of biochar, while oxygen can only form two oxygen-containing functional groups (C–O, C═O). This provides a basis for distinguishing the effects of water and oxygen on the oxygen-containing functional groups of biochar under plasma. From the TPD results, it was found that the sample after plasma treatment showed a peak of HgO at 300 °C. This indicates that the oxygen-containing functional group formed under plasma oxidised Hg^0. It is necessary to investigate which functional groups oxidised Hg^0 to determine the mechanism. Therefore, the XPS of RB-H-180 and RB-O-180 after Hg^0 adsorption was also tested. The two samples after adsorption of Hg^0 were designated RB-H-180 used and RB-O-180 used, respectively. For RB-H-180 used, C–O, C═O and O–C═O were consumed by 29.0%, 3.8%, and 1.8%, respectively. The RB-O-180 used only reduced the proportion of C–O by 13%. Therefore, the oxygen-containing functional groups formed by water and oxygen after plasma treatment were also inconsistent with respect to the oxidation characteristics of Hg^0.

In daily storage, biochar is inevitably exposed to the air. Based on the previous H_2O-TG and O_2-TPD results, biochar has the ability to adsorb water and oxygen from the air. Many experimental samples are used after a period of storage. Such samples undergo a change in oxygen-containing functional groups after plasma treatment. However, the dominant position of the adsorbed water and oxygen species to generate oxygen-containing functional groups under the plasma needs to be determined. RB stored for one month was subjected to N_2-plasma

treatment. The obtained sample was designated RB-N-1M. The XPS results of RB-N-1M are shown in Fig. 6 and Table 2. Compared to RB, the proportion of the two oxygen-containing functional groups of RB-N-1M was increased; one was C–O and the other was C═O. The proportion of C–O and C═O increased by 7.2% and 0.6%, respectively. The change in the oxygen-containing functional groups of RB-N-1M was similar to that of RB-O-180. The proportion of O–C═O in both did not increase. Therefore, it can be speculated that the oxygen adsorbed in the storage process dominates the formation of oxygen-containing functional groups under plasma treatment.

3.5. FTIR analysis

The specific generated oxygen-containing functional groups need to be revealed by FTIR. The FTIR results are shown in Fig. 7. The infrared spectra of three samples, i.e. RB, RB-H-180 and RB-O-180, are shown in Fig. 7(a). The peak at 1050 cm^{-1} is attributed to stretching vibration of Si-O of silicone. The peak at 3448 cm^{-1} is attributed to the expansion and contraction of liquid water [38–40]. As shown in Fig. 7(b), the spectra of RB-H-180 and RB-O-180 changed from 4000 to 3000 cm^{-1} compared with RB. For RB-H-180, a new peak appeared at 3300 cm^{-1}. This peak corresponds to the O–H stretching of the phenolic hydroxyl group [41,42]. For RB-O-180, the peak appearing at 3380 cm^{-1} corresponds to the O–H stretching of the alcoholic hydroxyl group [43]. It can be seen that the C-O formed on the biochar after the plasma treatment of water and oxygen belongs to different functional groups. As shown in Fig. 7(c), the peak intensities of RB-H-180 and RH-O-180 at 1645 cm^{-1} were stronger than those of RB. The peak at 1645 cm^{-1} corresponds to the C═O stretching of benzoquinone [39,41,44]. Therefore, the C═O generated on RB-H-180 and RB-O-180 should belong to benzoquinone. As shown in Fig. 7(d), only the peak shape of RB-H-180 had changed. The peak in the range of 1500 cm^{-1} to 1400 cm^{-1} differentiated into two peaks. The peak at 1430 cm^{-1} is in-plane bending vibrations of the C–OH of the carboxylic acid [41,45,46]. Combined with the XPS results, the O–C═O structure formed by RB-H-180 should be attributed to carboxylic acid.

3.6. Mechanistic analysis

From the above characterisation results, the oxygen-containing functional groups formed by the water and oxygen adsorbed in the biochar in plasma environment and the oxidation characteristics of the generated oxygen-containing functional groups to Hg^0 can be obtained.

First, the water physically adsorbed on the biochar is dissociated into active groups such as O*, OH*, H* under the action of plasma. Then, OH* is combined with C on the biochar benzene ring to form a phenolic hydroxyl group. OH* can also be formed by recombination of O* and H*. Benzoquinone is obtained by combining O* with C on the benzene ring. The source of the carboxyl group may be that O* and OH* bind to the C atom at the same time. In the adsorption experiment of mercury, Hg^0 is oxidised by these generated oxygen-containing functional groups to form HgO. Therefore, the process of water forming oxygen-containing functional groups on biochar in a plasma environment and the oxidation process of the obtained oxygen-containing functional group to Hg^0 can be expressed by the following equation.

$$2H_2O_{(ad)} \xrightarrow{Plasma} 3H* + O* + OH* \quad (2)$$

$$H* + O* \xrightarrow{Plasma} OH* \quad (3)$$

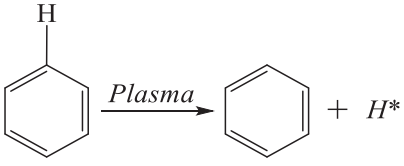

(4)

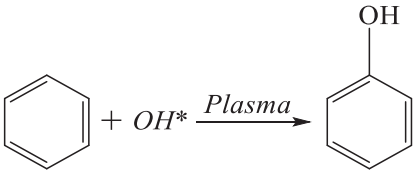

(5)

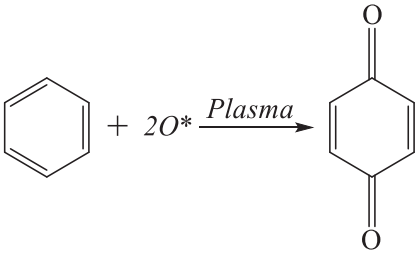

(6)

$$-C + O* + OH* \xrightarrow{Plasma} -COOH \quad (7)$$

$$Hg^0_{(g)} + Biochar \rightarrow Hg^0_{(ad)} \quad (8)$$

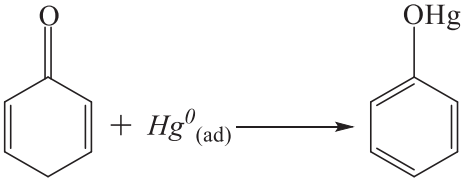

(9)

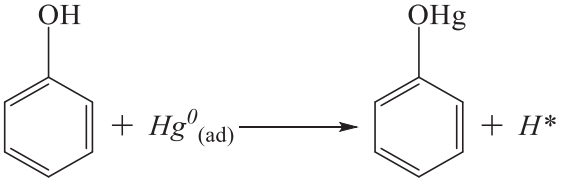

(10)

$$-COOH + Hg^0_{(ad)} \rightarrow -COOHg + H* \quad (11)$$

The oxygen adsorbed on the biochar is decomposed into active groups such as O* under the action of plasma. The C–H bond on the carbon surface is broken by the plasma, which releases H*. The C atom on the biochar combines with O* and H* to form an alcoholic hydroxyl. At the same time, O* also combines with the C atom on the benzene ring to form benzoquinone. According to the XPS results, the RB-O-180 mercury removal process consumes only C-O. Therefore, only the alcoholic hydroxyl group oxidises Hg^0 during the mercury removal process. Therefore, the process of oxygen forming oxygen-containing functional groups on biochar in a plasma environment and the oxidation process of the obtained oxygen-containing functional group to Hg^0 can be expressed by the following equation.

$$O_{2(ad)} \xrightarrow{Plasma} 2O* \quad (12)$$

$$-C - H \xrightarrow{Plasma} -C + H* \quad (13)$$

$$-C + O* + H* \xrightarrow{Plasma} -COH \quad (14)$$

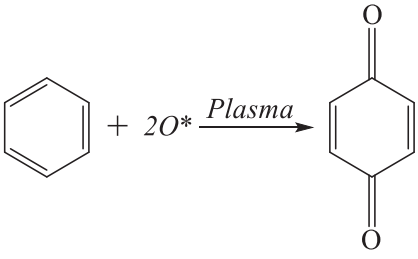

(15)

$$Hg^0_{(g)} + Biochar \rightarrow Hg^0_{(ad)} \quad (16)$$

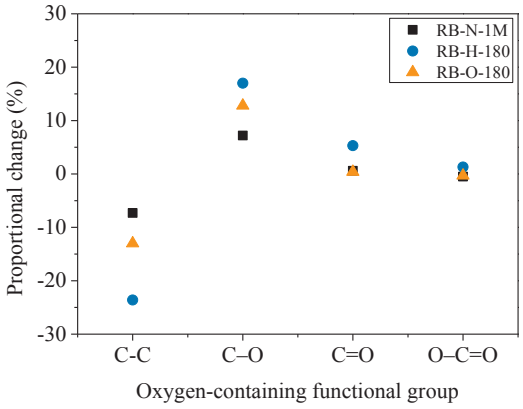

Fig. 8. Oxygen-containing functional group change trend distribution.

Table 3
Correlation analysis of XPS.

Sample	Percent change in oxygen-containing functional groups compared to RB (%)				Correlation coefficient
	C–C	C–O	C=O	O–C=O	
RB-N-1M	−7.3	7.2	0.6	−0.5	–
RB-H-180	–23.6	17.0	5.3	1.3	0.977
RB-O-180	−13.0	12.8	0.4	−0.3	0.999

$$-COH + Hg^{0}_{(ad)} \rightarrow -COHg + H* \quad (17)$$

It was found that water and oxygen produce different oxygen-containing functional groups on the surface of biochar in a plasma environment. Biochar inevitably absorbs water and oxygen from the air in everyday storage. This provides oxygen for plasma processing. According to the above results, both water and oxygen form oxygen-containing functional groups on the surface of the biochar in plasma environment. Therefore, for samples stored for a period of time, the dominant position of oxygen or water in the formation of oxygen-containing functional groups needs to be clarified.

A correlation analysis of the oxygen-containing functional group growth of RB-H-180 and RB-O-180 with RB-N-1M was carried out. The results of the correlation analysis are shown in Fig. 8 and Table 3. The value of the oxygen-containing functional group change in Table 3 was obtained by subtracting RB from the sample. The results show that the correlation coefficient between RB-H-180 and RB-N-1M was 0.977 and the correlation coefficient between RB-O-180 and RB-N-1M was 0.999. This indicates that the results of RB-O-180 are closer to those of RB stored for one month. In addition, the proportion of oxygen in the air is generally about 21.0%, and the proportion of water vapour does not exceed 0.1% [47]. Biochar is more likely to come into contact with oxygen in the air. Therefore, in the biochar storage process, the adsorbed oxygen dominates the formation of oxygen-containing functional groups during the plasma treatment. However, the correlation of RB-H-180 is also quite high. The role of physically adsorbed water in biochar in the plasma treatment cannot be ignored.

4. Conclusions

In this study, biochar adsorbed water or oxygen for different periods of time, and the mercury removal efficiency was tested after plasma treatment. These experiments showed that when too much water adsorbed by biochar, the mercury removal effect of biochar is inhibited. However, the plasma decomposes water into oxygen-containing free radicals, and these oxygen-containing free radicals combine with biochar to form oxygen-containing functional groups, thereby compensating for the inhibition of mercury removal. For biochar after oxygen adsorption, the plasma makes the biochar easier to sinter, thereby reducing its mercury removal efficiency. As the time required for adsorbing oxygen becomes longer, the more oxygen is enriched on the biochar. The abundant physical adsorbed oxygen is dissociated into oxygen-containing free radicals in a plasma environment. The free radical combines with biochar to form oxygen-containing functional groups. The mercury removal efficiency of the biochar increases as the oxygen adsorption time becomes longer. After plasma treatment, phenolic hydroxyl group, carboxyl group and benzoquinone carbonyl group are generated on the water adsorbed biochar while alcoholic hydroxyl group and benzoquinone carbonyl group are formed on the oxygen adsorbed biochar. The generated oxygen-containing functional group oxidises Hg^0 to HgO. Correlation analysis revealed that the oxygen adsorbed by the biochar from the air is the main source of oxygen-containing functional groups generated in a non-oxygen plasma environment. Therefore, in oxygen-free plasma, the main source of generated oxygen-containing functional groups on adsorbent is the oxygen adsorbed by the adsorbent during storage.

CRediT authorship contribution statement

Huicong Zhang: Methodology, Investigation, Writing - original draft. **Tao Wang:** Conceptualization, Methodology, Funding acquisition. **Wei-Yin Chen:** Writing - review & editing. **Yongsheng Zhang:** Supervision, Project administration. **Baomin Sun:** Writing - review & editing. **Wei-Ping Pan:** Writing - review & editing.

Declaration of Competing Interest

The authors declare that they have no known competing financial interests or personal relationships that could have appeared to influence the work reported in this paper.

Acknowledgements

This work was supported by National Natural Science Foundation of China (51706069) and the Fundamental Research Funds for the Central Universities (2019QN012). Wei-Yin Chen is grateful to the National Science Foundation Award of America (1632899) for its financial support.

References

[1] Asadullin TY, Galeev IG. The magnetic field application for the gas discharge plasma control in processes of surface coating and modification. J Phys Conf Ser 2017;012003. https://doi.org/10.1088/1742-6596/789/1/012003.
[2] Ashford B, Tu X. Non-thermal plasma technology for the conversion of CO_2. Curr Opin Green Sustainable Chem 2017;3:45–9. https://doi.org/10.1016/j.cogsc.2016.12.001.
[3] Muhammad A, Liao X, Cullen PJ, Liu D, Xiang Q, Wang J, et al. Effects of Nonthermal Plasma Technology on Functional Food Components: NTP effects on functional components. J Mater Eng Perform 2018;17(5):1379–94. https://doi.org/10.1111/1541-4337.12379.
[4] Yu J, Zhang L, Liu K, Lu L, Lu D, Zhou H. Effect of Pulse Detonation-Plasma Technology Treatment on T8 Steel Microstructures. J Mater Eng Perform 2017;26(12):6198–206. https://doi.org/10.1007/s11665-017-3067-y.
[5] Lu L, Zheng C, Chen J, Zhou J, Xiang G, Ni M, et al. Plasma-induced adsorption of elemental mercury on TiO_2 supported metal oxide catalyst at low temperatures. Fuel Process Technol 2015;138:14–20. https://doi.org/10.1016/j.fuproc.2015.04.021.
[6] Xiang Y, Xu Z, Zhou Y, Wei Y, Long X, He Y, et al. A sustainable ferromanganese biochar adsorbent for effective levofloxacin removal from aqueous medium. Chemosphere 2019;237:124464https://doi.org/10.1016/j.chemosphere.2019.124464.
[7] Xiang Y, Xu Z, Wei Y, Zhou Y, Yang X, Yang Y, et al. Carbon-based materials as adsorbent for antibiotics removal: Mechanisms and influencing factors. J Environ Manage 2019;237:128–38. https://doi.org/10.1016/j.jenvman.2019.02.068.
[8] Zhang H, Wang T, Sui Z, Zhang Y, Sun B, Pan W-P. Enhanced mercury removal by transplanting sulfur-containing functional groups to biochar through plasma. Fuel 2019;253:703–12. https://doi.org/10.1016/j.fuel.2019.05.068.
[9] Wang T, Liu J, Zhang Y, Zhang H, Chen W-Y, Norris P, et al. Use of a non-thermal plasma technique to increase the number of chlorine active sites on biochar for

improved mercury removal. Chem Eng J 2018;331:536–44. https://doi.org/10.1016/j.cej.2017.09.017.
[10] Zhang H, Wang T, Sui Z, Zhang Y, Norris P, Sun B, et al. Plasma Induced Addition of Active Functional Groups to Biochar for Elemental Mercury Removal. Plasma Chem Plasma Process 2019. https://doi.org/10.1007/s11090-019-10019-4.
[11] Wang T, Wu J, Zhang Y, Liu J, Sui Z, Zhang H, et al. Increasing the chlorine active sites in the micropores of biochar for improved mercury adsorption. Fuel 2018;229:60–7. https://doi.org/10.1016/j.fuel.2018.05.028.
[12] Zhang B, Xu P, Qiu Y, Yu Q, Ma J, Wu H, et al. Increasing oxygen functional groups of activated carbon with non-thermal plasma to enhance mercury removal efficiency for flue gases. Chem Eng J 2015;263:1–8. https://doi.org/10.1016/j.cej.2014.10.090.
[13] Bohli T, Ouederni A. Improvement of oxygen-containing functional groups on olive stones activated carbon by ozone and nitric acid for heavy metals removal from aqueous phase. Environ Sci Pollut Res Int 2016;23(16):15852–61. https://doi.org/10.1007/s11356-015-4330-0.
[14] Hoon Yang J, Yj Lee, Hee Kim Y, Hyun Moon S, Ho Ha B, Sook Shin Y, et al. Effects of N_2 on the Growth of Multiwalled Carbon Nanotubes Synthesized by Plasma-Enhanced Chemical Vapor Deposition. Jpn J Appl Phys 2003;42:6713–6. https://doi.org/10.1143/JJAP.42.6713.
[15] Majumdar A, Das SC, Ghosh B, Hippler R. Equivalent Dielectric property of hydrogenated carbon nitride film in CH_4/N_2 DBD plasma: Gas and Solid phase reaction. Int J Eng Sci Invent 2015;3(1):37–50.
[16] Wang T, Wan Z, Yang X, Zhang X, Niu X, Sun B. Promotional effect of iron modification on the catalytic properties of Mn-Fe/ZSM-5 catalysts in the Fast SCR reaction. Fuel Process Technol 2018;169:112–21. https://doi.org/10.1016/j.fuproc.2017.09.029.
[17] Chmielniak T, Słowik K, Sajdak M. Mercury removal by mild thermal treatment of coal. Fuel 2017;195:290–8. https://doi.org/10.1016/j.fuel.2017.01.073.
[18] Liu D, Zhou W, Wu J. Effect of Ce and La on the activity of CuO/ZSM-5 and MnOx/ZSM-5 composites for elemental mercury removal at low temperature. Fuel 2017;194:115–22. https://doi.org/10.1016/j.fuel.2016.12.076.
[19] Tan Z, Niu G, Chen X. Removal of elemental mercury by modified bamboo carbon. Chin J Chem Eng 2015;23(11):1875–80. https://doi.org/10.1016/j.cjche.2015.09.001.
[20] Zhao Y, Ma X, Xu P, Wang H, Liu Y, He A. Elemental mercury removal from flue gas by $CoFe_2O_4$ catalyzed peroxymonosulfate. J Hazard Mater 2018;341:228–37. https://doi.org/10.1016/j.jhazmat.2017.07.047.
[21] Gu Y, Zhang Y, Lin J, Zhang Z, Xu H, Norris P, et al. Homogeneous mercury oxidation with bromine species released from HBr-modified fly ash. Fuel 2016;169:58–67. https://doi.org/10.1016/j.fuel.2015.11.087.
[22] Zhu J, Zhao Z, Xiao D, Li J, Yang X, Wu Y. Study of $La_2-xSrxCuO_4$ (x = 0.0, 0.5, 1.0) catalysts for NO + CO reaction from the measurements of O_2-TPD, H_2-TPR and cyclic voltammetry. J Mol Catal A: Chem 2005;238(1):35–40. https://doi.org/10.1016/j.molcata.2005.03.036.
[23] Shan XL, Guan NJ, Zeng X, Chen J, Xiang SH. Studies on Cu-containing MFI zeolites by H_2-TPR and O_2-TPD. Chin J Catal 2001;22(3):237–41.
[24] Wang C, Zhang C, Hua W, Guo Y, Lu G, Gil S, et al. Catalytic oxidation of vinyl chloride emissions over Co-Ce composite oxide catalysts. Chem Eng J 2017;315:392–402. https://doi.org/10.1016/j.cej.2017.01.007.
[25] Zhang C, Wang C, Gil S, Boreave A, Retailleau L, Guo Y, et al. Catalytic oxidation of 1,2-dichloropropane over supported LaMnOx oxides catalysts. Appl Catal B 2017;201:552–60. https://doi.org/10.1016/j.apcatb.2016.08.038.
[26] Pakpum C, Pussadee N. Deep reactive ion etching of alumina titanium carbide using chlorine-based plasma. Surf Coat Technol 2016;306:194–9. https://doi.org/10.1016/j.surfcoat.2016.05.076.
[27] Ozaki M, Uddin MA, Sasaoka E, Wu S. Temperature programmed decomposition desorption of the mercury species over spent iron-based sorbents for mercury removal from coal derived fuel gas. Fuel 2008;87(17):3610–5. https://doi.org/10.1016/j.fuel.2008.06.011.
[28] Hassett DJ, Pflughoeft-Hassett DF, Mercury Laudal DL. Release from Coal Combustion By-Products to the Environment. Mercury in the Environment Specialty Conference 1999.
[29] Wu S, Uddin MA, Nagano S, Ozaki M, Sasaoka E. Fundamental Study on Decomposition Characteristics of Mercury Compounds over Solid Powder by Temperature-Programmed Decomposition Desorption Mass Spectrometry. Energy Fuels 2011;25(1):144–53. https://doi.org/10.1021/ef1009499.
[30] Li G, Wang S, Wang F, Wu Q, Tang Y, Shen B. Role of inherent active constituents on mercury adsorption capacity of chars from four solid wastes. Chem Eng J 2017;307:544–52. https://doi.org/10.1016/j.cej.2016.08.106.
[31] Lopez-Anton MA, Yuan Y, Perry R, Maroto-Valer MM. Analysis of mercury species present during coal combustion by thermal desorption. Fuel 2010;89(3):629–34. https://doi.org/10.1016/j.fuel.2009.08.034.
[32] Chen M. Study on Mercury Adsorption Form and Desorption Characteristics in Simulated Flue Gas. Southeast University 2017:32–40.
[33] Zhou J-H, Sui Z-J, Zhu J, Li P, Chen D, Dai Y-C, et al. Characterization of surface oxygen complexes on carbon nanofibers by TPD, XPS and FT-IR. Carbon 2007;45(4):785–96. https://doi.org/10.1016/j.carbon.2006.11.019.
[34] Shao D, Hu J, Wang X. Plasma Induced Grafting Multiwalled Carbon Nanotube with Chitosan and Its Application for Removal of UO_2^{2+}, Cu^{2+}, and Pb^{2+} from Aqueous Solutions. Plasma Processes Polym 2010;7(12):977–85. https://doi.org/10.1002/ppap.201000062.
[35] De Velasco Maldonado PS, Hernández-Montoya V, Montes-Morán MA. Plasma-surface modification vs air oxidation on carbon obtained from peach stone: Textural and chemical changes and the efficiency as adsorbents. Appl Surf Sci 2016;384:143–51. https://doi.org/10.1016/j.apsusc.2016.05.018.
[36] Lewin E, Persson POÅ, Lattemann M, Stüber M, Gorgoi M, Sandell A, et al. On the origin of a third spectral component of C1s XPS-spectra for nc-TiC/a-C nanocomposite thin films. Surf Coat Technol 2008;202(15):3563–70. https://doi.org/10.1016/j.surfcoat.2007.12.038.
[37] Zhang Y, Mei D, Wang T, Wang J, Gu Y, Zhang Z, et al. In-situ capture of mercury in coal-fired power plants using high surface energy fly ash. Environ Sci Technol 2019. https://doi.org/10.1021/acs.est.9b01725.
[38] Shen F, Liu J, Dong Y, Wu D. Mercury removal by biomass-derived porous carbon: Experimental and theoretical insights into the effect of H_2S. Chem Eng J 2018;348:409–15. https://doi.org/10.1016/j.cej.2018.05.019.
[39] Hadjittofi L, Pashalidis I. Uranium sorption from aqueous solutions by activated biochar fibres investigated by FTIR spectroscopy and batch experiments. J Radioanal Nucl Chem 2015;304(2):897–904. https://doi.org/10.1007/s10967-014-3868-5.
[40] Varga M, Izak T, Vretenar V, Kozak H, Holovsky J, Artemenko A, et al. Diamond/carbon nanotube composites: Raman, FTIR and XPS spectroscopic studies. Carbon 2017;111:54–61. https://doi.org/10.1016/j.carbon.2016.09.064.
[41] Weng S. Fourier transform infrared spectroscopy analysis. Chemical Industry Press; 2010.
[42] Chia CH, Gong B, Joseph SD, Marjo CE, Munroe P, Rich AM. Imaging of mineral-enriched biochar by FTIR, Raman and SEM–EDX. Vib Spectrosc 2012;62:248–57. https://doi.org/10.1016/j.vibspec.2012.06.006.
[43] Pehlivan E, Altun T, Cetin S, Iqbal Bhanger M. Lead sorption by waste biomass of hazelnut and almond shell. J Hazard Mater 2009;167(1):1203–8. https://doi.org/10.1016/j.jhazmat.2009.01.126.
[44] Šoštarić TD, Petrović MS, Pastor FT, Lončarević DR, Petrović JT, Milojković JV, et al. Study of heavy metals biosorption on native and alkali-treated apricot shells and its application in wastewater treatment. J Mol Liq 2018;259:340–9. https://doi.org/10.1016/j.molliq.2018.03.055.
[45] Bekiaris G, Peltre C, Jensen LS, Bruun S. Using FTIR-photoacoustic spectroscopy for phosphorus speciation analysis of biochars. Spectrochim Acta Part A Mol Biomol Spectrosc 2016;168:29–36. https://doi.org/10.1016/j.saa.2016.05.049.
[46] Bekiaris G, Bruun S, Peltre C, Houot S, Jensen LS. FTIR–PAS: A powerful tool for characterising the chemical composition and predicting the labile C fraction of various organic waste products. Waste Manage 2015;39:45–56. https://doi.org/10.1016/j.wasman.2015.02.029.
[47] H. Li Indoor air quality standards. Builders' Monthly, 2010; 31 (1): 35 doi: 10.3969/j.issn.1002-3232.2010.01.022.